Digital All-Optical Physical-Layer Network Coding

Charikleia Mitsolidou, Chris Vagionas,
Dimitris Tsiokos, Nikos Pleros and Amalia Miliou

Additional information is available at the end of the chapter

http://dx.doi.org/10.5772/intechopen.75908

Abstract

Network coding (NC) has recently attracted intense research focus for its potential to provide network throughput enhancements, security and reduced network congestions, improving in this way the overall network performance without requiring additional resources. In this chapter, the all-optical physical-layer network coding (AOPNC) technique is presented, focusing on digital encoding schemes that are based on optical XOR logical gates. It is also discussed how digital AOPNC can be implemented between sub-carrier-modulated (SCM) optical signals in radio-over-fiber (RoF) networks, circumventing the enhanced complexity arising by the use of SCM signals and the asynchrony that might exist between the data arriving at the encoding unit. AOPNC demonstrations are described for simple on/off keyed (OOK)-SCM data signals, as well as for more sophisticated higher-order phase modulation formats aiming to further improve spectrum efficiency and transmission capacity.

Keywords: all-optical physical-layer network coding (AOPNC), radio over fiber (ROF), millimeter wave communication, optical logic gates, semiconductor optical amplifier-Mach Zehnder interferometer (SOA-MZI)

1. Introduction

The explosive data traffic growth in combination with the increasing use of smart mobile devices has created the need for high-throughput wireless access networks at Gb/s scale [1, 2]. In this context, radio-over-fiber (RoF) networks have recently stepped in as a promising solution to satisfy this demand by seamlessly converging the ubiquity and mobility of the "last-meter" wireless networks with the high capacity of backhaul optical networks [3, 4]. Up to now, there are several RoF signal generation and modulation schemes [5, 6] as well as advanced functionalities

related to end-user mobility, hand-off schemes [7] and to network coding (NC) in RoF networks [8, 9]. Network coding (NC) has drawn significant scientific attention due to its capability to provide network throughput enhancements, security and low latency by improving the capacity resource utilization and enabling bidirectional data transport [10].

Until now, NC has been demonstrated separately for purely wireless networks [11] and passive optical networks (PONs) [12–14]. Regarding wireless networks, NC is performed at the relay by using conventional electronic processing of data, while most of the NC demonstrations in PONs rely on optical-electrical-optical (OEO) conversion before the encoding operation, resulting in further complexity at the central office (CO) and additional latencies to the overall communication [13, 15]. RoF technology was introduced as the technology that can merge wireless and optical functionalities via remote antenna units (RAUs) to deliver seamless communication between the wireless user and the CO. In order to comply with the requirements imposed by the trend of optical-wireless convergence, RoF technology should be able to implement unified NC between the optical network and the wireless user. Network coding concepts satisfying the earlier requirement are expected to enhance the overall network efficiency when implemented directly in the optical domain at the CO side.

However, till now, most of the optical PHY-layer NC (OPNC) demonstrations target the encoding of baseband optical signals transmitted in wired optical links. The cross-gain modulation (XGM) and cross-phase modulation (XPM) phenomena in semiconductor optical amplifiers (SOAs) and SOA-Mach Zehnder interferometers (SOA-MZIs) have been exploited to perform the XOR-based network coding between baseband on-off keyed (OOK) data signals [16, 17], while the four-wave mixing (FWM) phenomenon in SOA- [18] and highly-non-linear fiber (HNLF)-based XOR gates [19] has been employed for the encoding of differential phase shift keyed (DPSK) signals. Although all the aforementioned demonstrations provide performance enhancements in wired optical links, they are not suitable for RoF networks due their incapability to deal with the sub-carrier modulation (SCM) formats of the RoF signals and the possible asynchrony between the data arriving at the NC-encoding unit.

Up to now, only a limited number of physical-layer OPNC demonstrations are compatible with RoF networks [8, 9, 20]. These schemes utilize orthogonal polarization multiplexing and optical power addition yet favoring analog physical-layer NC in order to cope with the increased coding complexity associated with SCM RoF data signals. Recently, a digital AOPNC scheme for RoF networks that can perform a bitwise XOR function between OOK-SCM data has been demonstrated [21]. Moreover, the current trend in RoF networks is moving toward the use of phase modulation formats and high-order modulation [22, 23], aiming to improve the spectrum efficiency and transmission capacity. Therefore, digital AOPNC schemes compatible with DPSK- and differential quadrature phase shift keyed (DQPSK) phase-formatted SCM signals have been recently demonstrated for future radio-over-fiber (RoF) networks [24, 25].

In this chapter, a digital AOPNC demonstration for up to 2.5 Gb/s OOK data modulated over a 10 GHz SC is presented. The proposed experimental setup uses a SOA-MZI XOR gate as the all-optical encoder between two SCM-OOK data streams, exploiting the low-pass filtering response of a SOA-MZI [26] in order to process the data envelope while discarding the

10 GHz SC. For validation purposes, the optical encoding operation is further evaluated by deploying a second MZI-XOR gate to decode the signal and retrieve the original information.

To extend the use of this concept in more sophisticated modulation formats and in mm-wave communications [6, 7, 27], a digital AOPNC scheme for 60 GHz SCM DQPSK signals was also investigated with physical-layer simulations for a bit rate equal to 4Gb/s. The all-optical encoder, residing in the central office (CO), consists of a delay interferometer (DI) stage for the DQPSK-to-OOK conversion, a stage of SOA-MZI-based OOK-XOR gates followed by the SOA-MZI-based phase regenerator [28, 29] that forms the phase-encoded signal. A remote 60 GHz oscillator wavelength feeder is also incorporated in the NC unit to generate an additional wavelength spaced by 60 GHz to the encoded signal wavelength for allowing up-conversion through the beating at the receiver site [30]. An electrical XOR decoder was used in the simulations, emulating the decoding operation that would normally be performed at the wireless users' site, assuming wireless transmission by the RAU to the wireless user.

The rest of the chapter is organized as follows: Section 2 presents the proposed AOPNC-RoF-based conceptual scheme; Section 3 includes the setup and the results for the coding between two OOK-SCM signals; Section 4 presents the AOPNC setup and results for the DQPSK-SCM signals. Finally, conclusions are addressed in Section 5.

2. Concept overview

Figure 1 illustrates the proposed AOPNC-based RoF network, comprising the NC unit at the CO and the two wireless end users communicated with the respective RAUs, which in turn are connected with the CO via a fiber. Users A and B transmit their packets to the RAUs, where they are converted to SCM optical streams through the modulation of the laser diodes (LDs), coupled together and forwarded to the CO through the optical media. The physical layer all-optical XOR-encoding operation is performed on the fly at the CO and the resultant signal is broadcasted back to both RAUs, de-multiplexed from the uplink traffic and converted from optical-to-electrical (o/e) by means of a photodiode (PD). The electrical encoded signal is transmitted from each RAU to the respective wireless user in
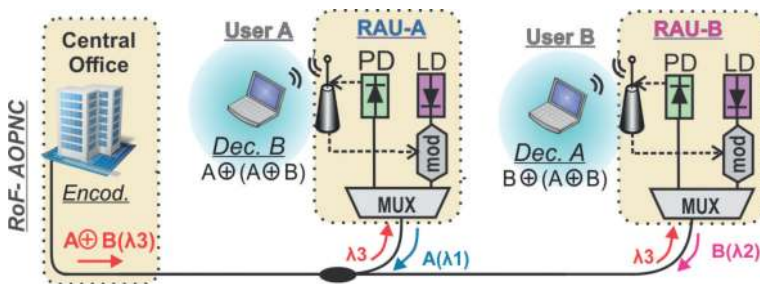

Figure 1. All-optical digital network coding (NC) scheme at the central office of RoF networks.

order to be decoded. Each user recovers the bit sequence originating from the other user by performing a second XOR function between its own locally stored data and the received NC-encoded data. In this way, the AOPNC technique implemented at the CO is capable of encoding information coming from users located in different cells, which is not feasible with current wireless NC schemes.

Figure 2(a) depicts the frame scheduling in an RoF network where no network coding is employed, as well as the frame scheduling in an RoF-NC-based communication scheme. In both cases, it is considered that for the uplink, RAU-A and B transmit data packets modulated on the wavelengths $\lambda 1$ and $\lambda 2$, respectively, while for the downlink traffic, the CO uses $\lambda 3$. When network coding is not employed, RAUs transmit Data A and B to the CO during the first timeslot, while the CO receives both packets and forwards packet from user A to B and packet from user B to A, using two successive timeslots. When **n**etwork **c**oding is applied in a**n** RoF network, then the CO encodes and broadcasts the NC-encoded packet to both users in a single timeslot, occupied only two timeslots for the uplink and downlink traffic. This concept exploits the pre-amble and post-amble of the frames [31] for packet order resolving in case of non-synchronized packets. **Figure 2(b)** shows the encoding and decoding operation when packets from **u**ser A and B reach the encoding unit at the CO bit level synchronized or with a time delay equal to Δt (asynchronous operation). In the case of synchronous operation, data from **u**ser A and B are digitally encoded by means of a SOA-MZI XOR gate and broadcasted to both users. Each user recovers the packet of the other user by performing a second bitwise XOR operation between the received encoded signal and its own data. Considering that the end users are wireless clients that may reside at different distances from their respective RAUs resulting even to sub-bit time mismatch between the two packet**s** reaching the CO, it is critical for the AOPNC scheme to operate also for asynchronous data.

As shown in **Figure 2(b),** during asynchronous operation, a sub-bit optical pulse with duration equal to Δt is generated in the encoding packet. However, the final decoded packets from the second XOR operation can still be correctly recovered by both end users through a second XOR operation, without any data loss.
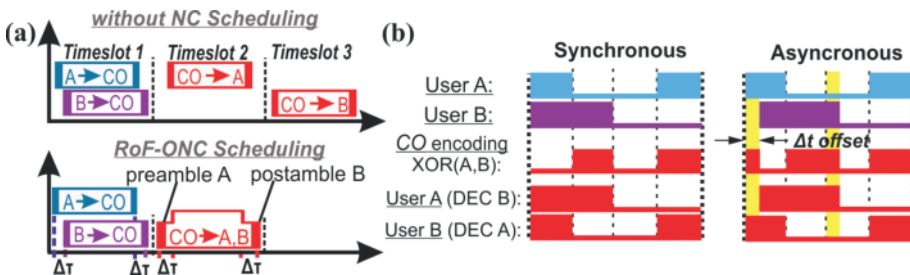

Figure 2. (a) Frame scheduling for RoF network: Without network coding and with the proposed AOPNC scheme and (b) conceptual encoding and decoding operation for synchronous and asynchronous data with a time offset of a sub-bit delay Δt.

3. Digital all-optical physical-layer network coding for OOK-SC signals

3.1. Experimental setup

Figure 3 shows the experimental configuration, exploiting two SOA-MZI gates, the first for the encoding process at the CO and the second for decoding XOR operation that in a realistic RoF is performed at the end user. The continuous wave (CW) signals at $\lambda 1 = 1549.8$ nm, $\lambda 2 = 1553.1$ nm and $\lambda 3 = 1553.6$ nm were emitted by three tunable LDs (TLDs), multiplexed by an array waveguide grating (AWG) and modulated by an electro-absorption modulator (EAM) by a 10 GHz electrical clock signal for the SC generation. The output of the EAM was amplified by an erbium-doped fiber amplifier (EDFA) and de-multiplexed by means of an AWG. Signals $\lambda 1$ and $\lambda 2$ were further OOK modulated by two LiNbO$_3$ modulators, which were driven by a programmable pattern generator (PPG) loaded with 2.5 Gb/s NRZ 2^7–1 pseudo random bit sequence (PRBS), so as to form the SCM-OOK uplink data A and B signals. These uplink signals were transmitted through spools of single-mode fibers (SMF) with lengths of 3.9 km and 4 km, emulating the uplink connections between the RAUs and CO. An optical delay line (ODL) was employed at the branch carrying the data B stream, in order to enable bit-level synchronization during synchronous operation and insert time offsets at the asynchronous operation. Stream $\lambda 3$ was not modulated with data in order to emulate the SC produced at the CO and used for the downlink traffic. Variable optical attenuators (VOAs) and polarization controllers (PCs) were also employed for power regulation and polarization adjustments, respectively.

The data streams ($\lambda 1$, $\lambda 2$) were injected into the control ports A and D, while $\lambda 3$-SC was applied at the port C of the SOA-MZI XOR gate 1. The input power levels were measured, 800 µW(−1 dBm) for $\lambda 1$, $\lambda 2$ and 400 µW(−4 dBm) for $\lambda 3$. The SOA-MZI was biased in such a way so that port G acts as the switching port. Hence, when only one of the two data is present, a π shift between the two SOA-MZI branch signal constituents is obtained by cross-phase modulation (XPM) and $\lambda 3$ emerges with a logical "1" at the output port G. Otherwise, when both data signals are equally present, then $\lambda 3$ bears a logical "0", confirming the implementation of an all-optical XOR gate by means of an SOA-MZI. The output port of the first XOR encoding gate was filtered and launched into port D of the second SOA-MZI XOR gate, which
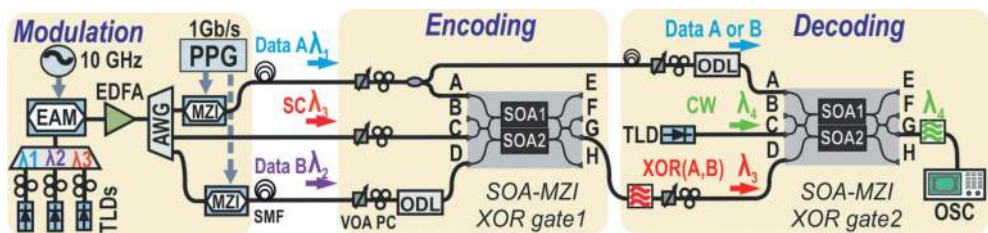

Figure 3. Experimental setup of the proposed AOPNC scheme comprising the SC-modulated data generation, the encoding and the decoding process.

acts as a decoder. A part of data A was connected with port A for decoding data B, while a CW signal launches port C ($\lambda 4 = 1548.4$ nm). Equivalently, when data A is decoded, data B is connected to port A of the second SOA-MZI. The input power levels were measured, −1 dBm for the control signals $\lambda 1$, $\lambda 3$ and − 4 dBm for $\lambda 4$. SMF and ODL were used for pattern and bit-level synchronization. The output of the XOR2 gate was filtered by a 0.65 nm filter and monitored by an optical sampling oscilloscope (OSC).

The SOA-MZIs featured two 1600 μm long hybrid-integrated SOAs, both operating at a moderate current value of 180 mA. The SOA gain recovery value at driving conditions was 180 ps for both SOA-MZI XOR gates, significantly longer than the 100 ps period of the SC signal. In this way, the SOA-MZI response of both XOR gates is turned into a low-pass filtering [26], neglecting the high-speed sub-carrier of the optical control data A and B signals but correctly processing their data envelopes.

3.2. Experimental results for synchronous operation

Figure 4 presents the experimental results obtained for the synchronous encoding and decoding operations between two 2.5 Gb/s data streams. **Figure 4(a)** and **(b)** shows the input time traces of data A and B, respectively, while the XOR stream at the output of the first SOA-MZI is shown in **Figure 4(c)**. The encoded stream features a logical "1" bit value when data A and B correspond to different bit values, while it is equal to "0" when the two data have the same logical bit value. **Figure 4(d)** and **(e)** illustrates the decoded data A and B at the output of the second SOA-MZI, after the XOR operation between the encoded signal and either the data B or data A, respectively. It should be noted that the decoded streams featured sub-bit dips
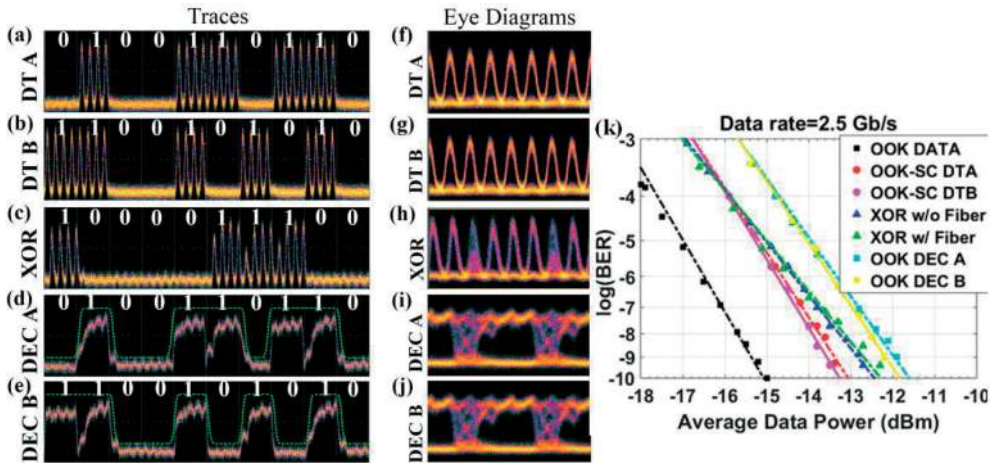

Figure 4. Experimental results for 2.5 Gb/s data. Traces (400 ps/div): (a) data a, b) data B, (c) encoded XOR, (d) decoded data a and (e) data B. Eye diagrams (80 ps/div): (f) data a, (g) data B, (h) encoded XOR, (i) decoded data a and (j) decoded data B. (k) BER curves for the OOK data without SC, the OOK-SC data, the encoded XOR with/without fiber after the users and the decoded output OOK data.

between successive "1"s, resulting from the XOR operation when logical "1"s are generated by the transition from differential phase $+\pi$ between the SOA-MZI branches to $-\pi$. However, the initial data patterns were retrieved successfully, confirming the successful decoded process at 2.5 Gb/s. **Figure 4(f)** and **(g)** depicts the eye diagrams of the input OOK-SCM data A and B, respectively. **Figure 4(h)** shows the eye diagram of the XOR-encoded signal at the output of the first SOA-MZI, exhibiting an extinction ratio (ER) of 9.6 dB and an amplitude modulation (AM) of 0.5 dB. **Figure 4(i)** and **(j)** illustrates the eye diagrams of the decoded data A and B, respectively, exiting the second SOA-MZI XOR gate. Both eye diagrams exhibit an ER equal to 8.2 dB and an AM equal to 1.2 dB.

The successful encoding and decoding operations were also verified with the aid of bit error rate (BER) measurements. **Figure 4(k)** shows the BER curves carried out at various stages of the system. The BER curves reveal error-free operations for both decoded data signals, having a power penalty equal to 3.2 dB when compared with the initial OOK data signals at BER = 10^{-9}. This power penalty is partially attributed to the SC modulation of data A and B, which introduces a power penalty of 2 dB. BER curves for the encoded XOR stream exiting the first SOA-MZI were also carried out for two cases: when the SCM-OOK DATA are directly inserted to the encoder without the use of extra fiber and when fiber spools of 3.9 km and 4 km are inserted between the OOK-SC data A and B and the first XOR gate in order to emulate the uplink connection. The power penalty between these two BER curves (with and without fiber) is negligible. By comparing the XOR curves with the OOK SCM data, the power penalty at 10^{-9} is approximately 0.7 dB.

3.3. Experimental results for asynchronous operation

Possible asynchrony between the two data streams reaching the encoding unit was also examined by introducing various sub-bit temporal delays at data B, as may potentially be introduced by mobile wireless users. **Figure 5(a)** and **(b)** illustrates the input traces of OOK-SC data A and the delayed-by-100-ps (0.25 τ_{bit}) data B, while **Figure 5(c)** depicts the encoded XOR trace. Although short "parasitic" pulses of 0.25 bit duration appear at the encoded XOR stream, by implementing the decoding XOR function between the encoded XOR and the delayed data B, the trace of the decoded data A can be successfully retrieved, as shown in **Figure 5(d)**. **Figure 5(e)** shows that data B was also correctly decoded by the XOR operation between the encoded stream and data A, after a time delay of 0.25 bit duration.

Similar results were obtained for the asynchronous encoding and decoding of NC operation where data B is delayed by a sub-bit time offset equal to 200ps (0.5 τ_{bit}), as shown in **Figure 5(f)–(j)**. **Figure 5(f)** and **(g)** illustrates the SCM-OOK data A and B, respectively, reaching the encoding XOR gate with a time offset of 200 ps. **Figure 5(h)** shows the encoded XOR trace exiting the first SOA-MZI, while **Figure 5(i)** and **(j)** shows the decoded data A and B after the second XOR operation between the encoded pattern and the initial data pattern of data B or A, respectively. In this operation, both data A and B were successfully retrieved, with decoded data B having a delay equal to the time offset. The highlighted insets magnify the traces in a specific part of the stream where the asynchrony can be observed and the XOR signal appears to have "parasitic" pulses equal to the respective time offsets.
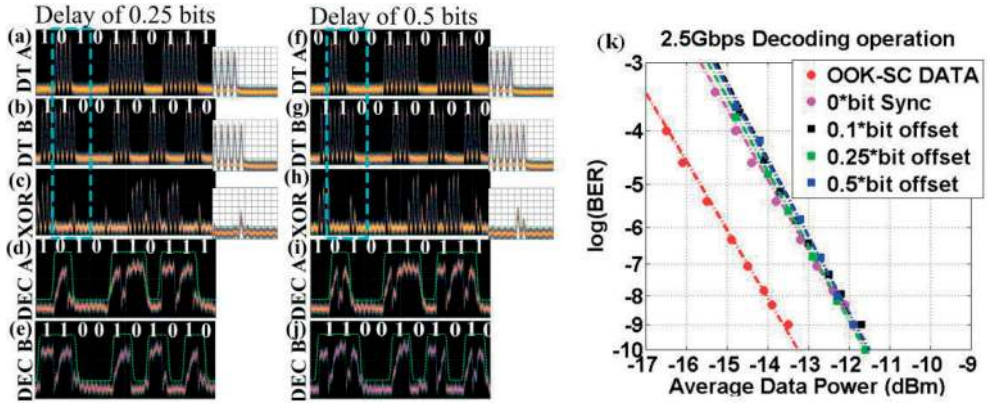
Figure 5. Experimental time traces of asynchronous 2.5 Gb/s operation for two different time offsets. Time traces (400 ps/div): For time offset equal to $0.25 \times \tau_{bit}$: (a) data a, (b) data B delayed by 0.25 bit, (c) encoded XOR signal, (d) decoded data a and (e) data B. For time offset equal to $0.5 \times \tau_{bit}$: (f) data a, (g) data B delayed by 0.5 bit, (h) encoded XOR signal, (i) decoded data a, (j) data B. Magnified insets highlight time offset. (k) BER curves of the decoded data signal for various time offsets between the input OOK-SC data.

The successful asynchronous operation was also evaluated with BER measurements, by inserting various relative delays between the two data and measuring the error rate for the down-converted decoded signal. **Figure 5(k)** shows the BER curves versus the average received power for time offsets equal to 0 τ_{bit}, 0.1 τ_{bit}, 0.25 τ_{bit} and 0.5 τ_{bit}, revealing error-free operation at 10^{-9} for all these cases. No additional power penalty when comparing the synchronous with the asynchronous operation was observed. This fact indicates that the performance of the proposed system remains functional even in the case of non-synchronized packets. The power penalty of the decoded stream with respect to the original down-converted OOK-SCM data is approximately 1.5 dB.

4. Digital all-optical physical-layer network coding for DQPSK-SC signals

4.1. Simulated setup

Figure 6 illustrates the setup employed in order to evaluate the proposed AOPNC scheme in an RoF network that uses DQPSK-SCM data signals. The data A and B streams are modulated employing the DQPSK format in the wireless users' transmitter (Tx) and transmitted to the RAUs for electrical-to-optical conversion. The CWs at $\lambda 1 = 1551$ nm (RAU A) and $\lambda 2 = 1553$ nm (RAU B), exiting the respective laser diodes (LDs), are modulated by the RF DQPSK signals via the MZMs. These signals are transmitted through a 4 km spool of SMFs, amplified by EDFAs and multiplexed by an AWG before entering the encoder in the CO premises. In the NC encoding unit, the data signals are inserted in two delay interferometers (DIs) in order to recover the OOK-u and -v complementary components. The differential optical phase between
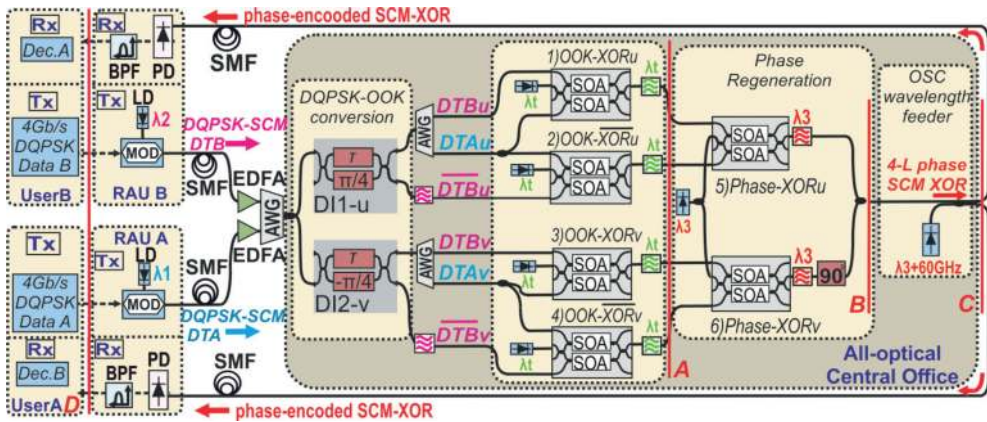
Figure 6. Simulated setup of the proposed AOPNC scheme comprising the two users, the respective remote antenna units (RAUs) and the all-optical encoding unit at the central office. Stages A–D are the stages where the OOK-XOR (XOR), the four-level phase-formatted XOR and the four-level phase-formatted optical and electrical SCM-XOR signals are generated, respectively.

DI1-u and DI2-v arms is set to 45 and −45° so as to recover the u- and v-constituents of data A and B, respectively. The u and v components correspond to the PRBS sequences before the differential encoding to I and Q bits as it is explained by Vorreau et al. [28].

The upper output port of each DI is connected with an AWG that de-multiplexes Data A and B signals, while the output of the DI's lower port is filtered by a band pass filter (BPF) with a center frequency equal to $\lambda2$ that keeps the OOK-SCM $\overline{DataB}$ and ignores the OOK-SCM data A. The OOK-converted streams are inserted into the control ports of the OOK-XOR gates based on SOA-MZIs and a continues wave λt (temp)=1555nm was inserted in their probe port. The data A-u and B-u are injected into the first SOA-MZI so as the OOK-XORu signal to be generated at the output switching port. The data A and $\overline{DataBu}$-constituents are applied at the second SOA-MZI forming the OOK–$\overline{XORu}$ at the output of the switching port. Similarly, the OOK-XORv and OOK–$\overline{XORv}$ are obtained at the output ports of the third and fourth MZIs, respectively. All the OOK encoded signals are then filtered and driven to the phase regeneration stage where the amplitude-to-phase conversion is performed by means of two SOA-MZIs. Particularly, the OOK-XORu and OOK–$\overline{XORu}$ are inserted into the control port of the fifth SOA-MZI and a continues wave in $\lambda3$=1557.36 nm was launched in the probe input port. The relative phase in the SOA arms was controlled by a high-level bit either in the OOK-XORu or the OOK–$\overline{XORu}$ arm, forming in this way the phase-encoded signal between data A-u and B-u components [28, 29]. Equivalently, the OOK-XORv and OOK–$\overline{XORv}$ streams are injected in the control arms of the lower SOA-MZI, forming the phase- and wavelength ($\lambda3$)-converted XORv signal. The phase-formatted XORu and XORv output streams are filtered and recombined with a relative phase shift (PS) of 90° so as to form the four-level (4-L) phase-formatted XOR signal. Finally, the phase regenerator output at $\lambda3$ is coupled with a coherent CW at $\lambda3$+60GHz generated by the remote 60GHz oscillator (OSC) wavelength feeder [31]. The phase-formatted XOR signal is sent via SMFs of 4 km to the RAU receiver (Rx) where it

was converted to RF data by utilizing the beating at the PD [31]. The output is filtered by a BPF centered at 60 GHz and transmitted through an assumed wireless link to the user's Rx, where the electrical decoding is performed.

Figure 7(a) presents the user's Tx which produces the DQPSK-SCM data signal. Each user's Tx comprises a PPG loaded with a 4 Gb/s NRZ 2^7–1 PRBS, so as to form the electrical data. A serial-to-parallel distributor is fed with the output stream of the PPG and synchronously splits it into the two output streams (u and v), each having a data rate of 2Gb/s, resulting in a total bit rate equal to 4 Gb/s. The DQPSK differential encoding unit converts the u- and v-constituents into the respective I and Q signals, which then are inserted into the electrical phase modulators (PMs) to modulate the 60 GHz signal coming from a local oscillator (LO). RF signals coming from the LO have a relative phase difference of 90°, so as the DQPSK-RF signal to be generated after the combination of the phase-formatted I and Q streams.

Figure 7(b) depicts the user's Rx that is responsible for the down-conversion and the decoding of the incoming NC-encoded stream. Each user's Rx receives the phase-encoded XOR signal from the RAU and splits it into two identical signals. Those signals are multiplied with the respective in-phase signals originating from the LO and having a relative phase difference of 90°. The phase matching of the 60 GHz signals coming from the LO and the splitter is achieved by the phase shifters (PSs). The power regulation of the down-converted OOK u- and v-constituents, exiting the multiplier, is provided by a DC source. The resultant signals are filtered by low-pass filters (LPFs) and inserted in the electrical XOR gates where the decoding process is performed by the XOR operation between the NC encoding signals and a local copy of user's data. In this way, user A extracts the data B
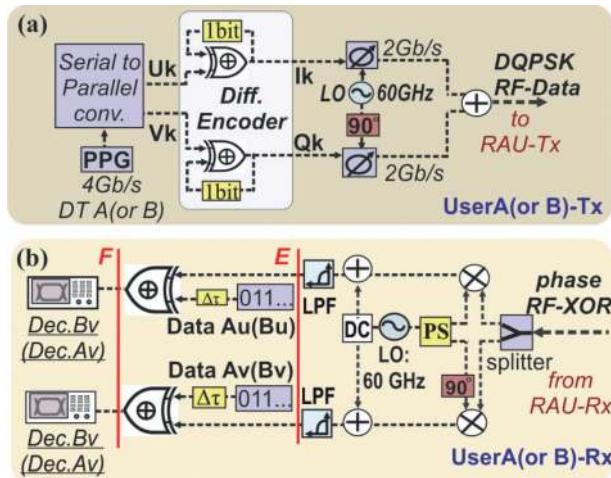

Figure 7. (a) Setup of the users' transmitter (Tx) generating the DQPSK-RF data and (b) setup of the users' receiver (Rx) performing the decoding operation. Stages E and F are the stages where the down-converted XOR-u (XOR-v) and the final decoded data signals are generated, respectively.

constituents, while user B decodes the data A u and v streams. The synchronization of the NC encoding signals and the user's data is achieved by the use of a time delay ($\Delta\tau$).

The simulations were carried out with the VPI photonics software suite [32], using as input the response of a custom-made SOA-MZI model [33] that matches the experimental measured response of a 1600-µm long hybrid-integrated SOA. The input power levels that were used were −1 dBm for the control signals and −4 dBm for the probe light, for all OOK SOA-MZIs. Both SOAs of the OOK-XOR and OOK–$\overline{\text{XOR}}$ MZI gates were driven by current values of 250 mA and had a recovery time of 100 ps, significantly longer than the 16.67 ps period of the 60 GHz SC. The SOAs of the phase regeneration XOR gates are driven by a 300 mA DC current and had an 80 ps recovery time.

4.2. Simulated results for synchronous operation

Figure 8 shows the time traces, eye diagrams and spectra obtained at various stages of the network coding-based 2 Gbaud RoF link during synchronous operation. The indicative patterns used for the simulation results are "1011111001" and "1010100110" for the u- and v- components of data A, while "1011010110" and "0100001100" were used for the data Bu
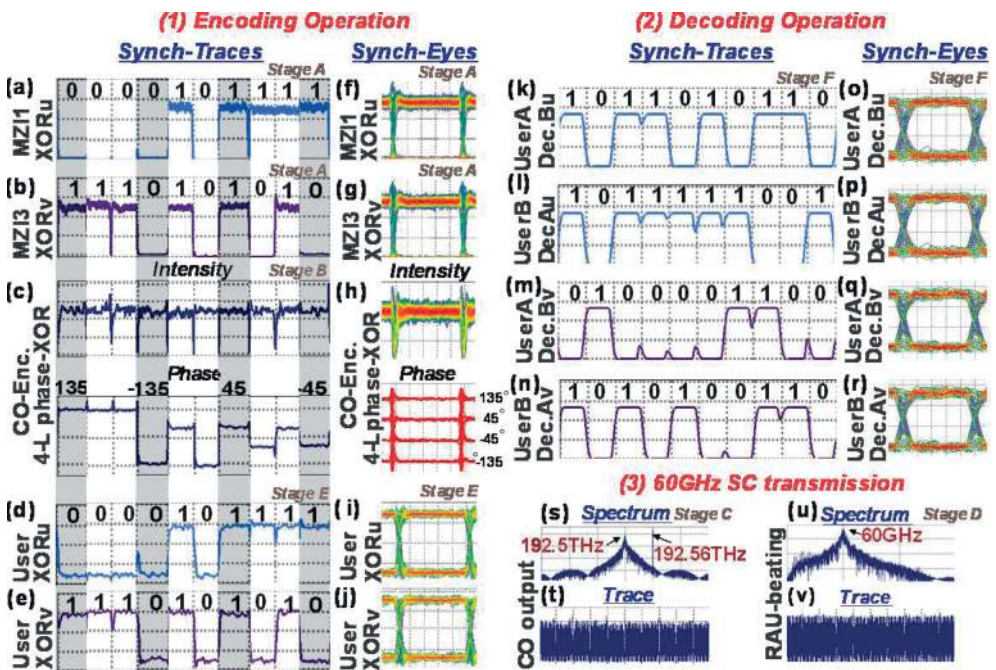

Figure 8. Results for synchronous AOPNC operation: (a)–(e) time traces of the encoding operation, (f)–(j) respective eye diagrams of encoding operation, (k)–(n) time traces of the decoding operation, (o)–(r) respective eye diagrams of decoding operation, (s) spectrum and (t) time trace of the SCM encoding signal at the CO's output and (u) spectrum and (v) time trace of the SCM RF encoding signal at the output of the RAU's Rx. 500 ps/div (traces) and 100 ps/div (eye diagrams).

and Bv components, respectively. **Figure 8(a)** and **(b)** shows the OOK-XORu and OOK-XORv time traces exiting the SOA-MZI-1 and SOA-MZI-3, respectively. Pulses are observed in the XOR streams, when data A and B constituents have different logical bit representations, while the power level is equal to 0 when data A and B exhibit the same logical value. The intensity and phase traces of the NC-phase-formatted stream at the output of the regenerator are shown in **Figure 8(c)**. The intensity envelope reveals a constant "high" power level, with small duration sub-bit dips generated by the transition of the differential phase between the SOA-MZI-5 and SOA-MZI-6 branches from +90° to −90°. The phase time trace presents the NC phase-encoded resultant signal, whose optical phase φ can take one of the four values: [−135, 135,−45 and 45°], corresponding to the logical bit pairs: "XORu, XORv"= ["00", "01", "10" and "11"], respectively. The grey markers highlight the encoding scheme, where the absence of the OOK-XORu and –XORv pulses is imprinted as −135°, the XORv pulses as 135°, the XORu pulses as −45° and the existence of both XORu, XORv pulses as 45°. **Figure 8(d)** and **(e)** depicts the electrical OOK down-converted XORu and XORv streams at the output of the low-pass filter (LPF) in the end-user receiver. These traces confirm the successful conversion of the four-level phase-formatted XOR signal to two binary NRZ-OOK XORu and XORv streams.

Figure 8(f) and **(g)** illustrates the eye diagrams of the OOK-XORu and XORv components exiting the SOA-MZI-1 and SOA-MZI-3. The eye diagrams exhibit an ER equal to 11.7 dB, an AM of 1.1 dB, a pulse overshoot (PO) of 1.4dB and a jitter of 23ps, showing a limited impact of pattern effects, stemming from the signal processing by SOAs. **Figure 8(h)** depicts the intensity eye diagram and the phase eye diagram of the NC-encoded phase-formatted signal exiting the phase regenerator. The intensity eye diagram exhibits an AM equal to 1.8 dB and a PO of 2.1 dB, while the respective phase eye diagram shows the four different phase levels of the encoded signal, revealing a relatively small-phase fluctuation of 1.5° from the expected phase values. In both diagrams, small duration dips at the beginning of the symbol pulse are observed, without yielding, however, any data loss. **Figure 8(i)** and **(j)** shows the eye diagrams of the electrical down-converted OOK XORu and XORv signal streams at the output of the LPF in the end-user Rx. The binary OOK XOR signals reveals an ER, AM, PO and jitter equal to 9 dB, 0.7 dB, 0.9 dB and 32 ps, respectively.

Figure 8(k) and **(l)** illustrates the decoded data Bu and Au streams, while **Figure 8(m)** and **(n)** depicts the complementary decoded data Bv and Av traces, each generated by the bitwise XOR between the NC-encoded XOR trace and the local copy of the user's data pattern. **Figure 8(o)** and **(p)** shows the eye diagrams of the decoded data Bu or Au signals, reporting an open eye with an ER, AM and jitter equal to 8.7 dB, 1.1 dB and 40 ps, respectively, with the dips appearing at the beginning of the pulses. Similarly, **Figure 8(q)** and **(r)** depicts the eye diagrams of the decoded data Av and Bv, respectively, both exhibiting an ER of 8.7 dB, an AM of 1.1 dB and a jitter of 40 ps.

Figure 8(s) represents the optical spectrum of the phase-encoded signal at the output of the CO after the coupling of the four-level XOR signal with a continuous wave coming from the 60 GHz OSC wavelength feeder. The phase-formatted signal has a center wavelength of λ3=1557.36nm (192.5 THz), while the continuous wave is emitted at the wavelength of 1556.88 nm (192.560 THz), resulting in a frequency spacing equal to 60 GHz. The time trace at the same stage is illustrated in **Figure 8(t)**, showing an envelope with a constant power level,

modulated by the sub-carrier of 60 GHz. **Figure 8(u)** shows the electrical spectrum of the beating signal at 60 GHz, produced by the photodiode and sent to the receiver of the end-user, while **Figure 8(v)** illustrates the respective time trace, showing the oscillations of the 60 GHz electrical signal below the constant power envelope.

4.3. Simulated results for asynchronous operation

In this section, the asynchronous operation was evaluated for different sub-bit time offsets between the two data signals. **Figure 9** includes the time traces and eye diagrams of the asynchronous encoding and decoding operation for a time offset of 0.5 of the symbol time duration (250ps). **Figure 9(a)** shows the OOK-XORu stream, generated after the XOR operation between the data Au and the delayed by 250 ps data Bu constituents at the output of the SOA-MZI-1, while **Figure 9(b)** illustrates the OOK-XORv signal exiting the SOA-MZI-3. As it is highlighted by the grey markers, the data asynchrony generates sub-bit pulses and dips at the encoded streams, which are said to be "interrupted". **Figure 9(c)** illustrates the intensity and phase traces of the four-level phase-formatted XOR signal exiting the regeneration stage after the recombination of the binary phase-XORu and phase-XORv signals. The intensity trace exhibits a constant power envelope with small duration sub-bit dips generated from the
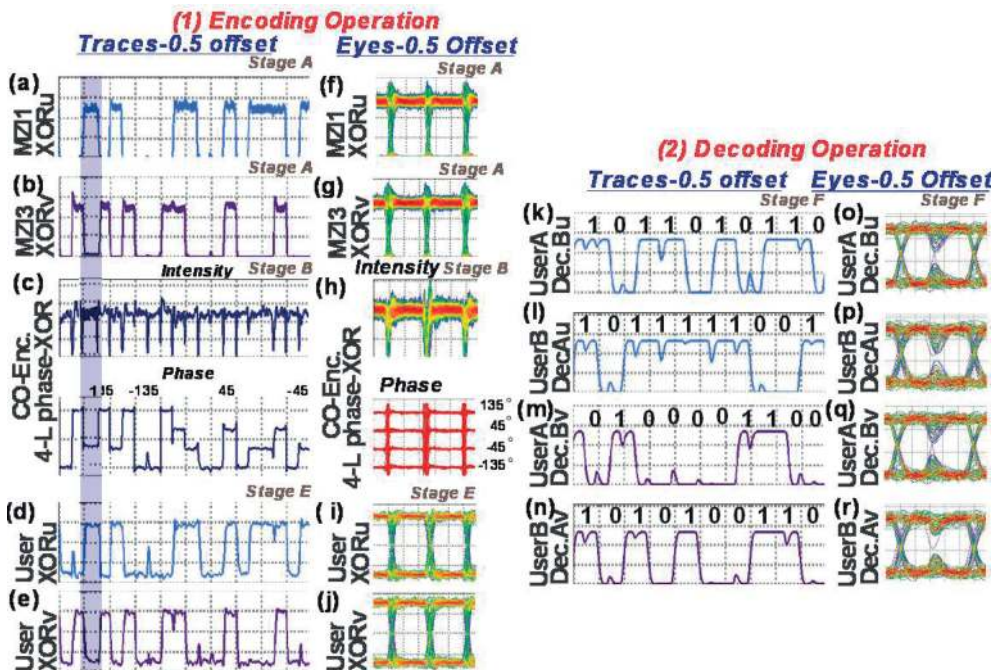

Figure 9. Results for the asynchronous AOPNC operation with a temporal offset equal to $0.5\tau_{bit}$: (a)–(e) time traces of the encoding operation, (f)–(j) respective eye diagrams of encoding operation, (k)–(n) time traces of the decoding operation, (o)–(r) respective eye diagrams of decoding operation. 500 ps/div (traces) and 100 ps/div (eyes).

transitions of the differential phase from +90° to −90° between the SOA-MZI-5 and/or SOA-MZI-6 branches. The phase trace shows the four different phase levels of the encoded signal, exhibiting sub-bit phase pulses and dips with a duration equal to 250 ps. **Figure 9(d)** and **(e)** depicts the XOR-u and XOR-v signals that were at the same time OOK- and down-converted by multiplying the received XOR streams with the respective in-phase 60 GHz signals generated by the LO at stage E.

Figure 9(f)–(j) shows the eye diagrams of the asynchronous encoding process. Particularly, **Figure 9(f)** and **(g)** illustrates the eye diagrams of OOK-XOR-u and XOR-v streams for a temporal offset equal to 0.5, exhibiting an ER of 11.7 dB, an AM of 1.1 dB, a PO of 1.4 dB and a jitter of 25 ps. As shown, an intersection is observed at both eye diagrams after a time delay equal to 250 ps from the beginning of the pulse. This intersection that has a jitter equal to 21 ps is formed by both sub-bit pulse falls and risings during the asynchronous XOR operation. **Figure 9(h)** illustrates the intensity and phase eye diagrams of the NC-phase-encoding signal at the output of the regenerator. An intensity envelope with an AM of 1.8 dB and PO of 2.1 dB is shown, exhibiting sub-bit dips when the relative phase of SOA-MZI-5 and/or SOA-MZI-6 is changed from 90 to −90° and vice versa. The respective phase eye diagram shows the four different phase levels of the encoded signal, revealing a small phase fluctuation equal to 1.5°. The electrical eye diagrams of the down-converted OOK-XORu and XORv signals at the users' Rx are depicted in **Figure 9(i)** and **(j)**, revealing an ER, AM, PO and a jitter equal to 9, 0.7, 0.9 dB and 32 ps, respectively.

Figure 9(k)–(r) shows the time traces and eye diagrams of the asynchronous decoding operation. **Figure 9(k)** and **(l)** depicts the decoded data Bu and Au components after the digital XOR operation between the encoded pattern of XORu and the initial pattern either of data Au or data Bu at the users A and B Rx, respectively. Similarly, **Figure 9(m)** and **(n)** illustrates the decoded data Bv and Av at the user A and B receivers, respectively. In that operation, it is shown that despite the interruptions which appear as "parasitic" pulses or dips at the NC-encoded signals, both the components of data A and B were at the end correctly recovered with the decoded data B components having a delay equal to the time offset. **Figure 9(o)** and **(p)** depicts the eye diagrams of the decoded data Bu and Au, respectively, both exhibiting an ER of 8.7 dB, an AM of 1.1 dB and jitter of 40 ps, with short duration dips and spikes appearing after time delay equal to 250 ps from the beginning of the symbol. Similarly, **Figure 9(q)** and **(r)** shows the eye diagrams of the decoded data Bv and Av, reporting similar eye characteristics (ER=8.7 dB and AM=1.1 dB, jitter=40 ps).

The asynchronous decoding operation was evaluated by carrying out BER measurements. **Figure 10(a)** shows the BER measurements versus the received RF power, for the decoded Au and Bu streams, when the time offset between the two data is equal to 0.25, 0.5 and 0.75 of the symbol duration. All BER curves show error-free operations at 10^{-9}. The BER curves reveal similar performance between synchronous and asynchronous operation, owing to the dips and spikes that were present at the edge of the pulse during synchronous operation being shifted within the duration of the pulses, however, without affecting the other pulse characteristics, such as ER, AM, PO, jitter and noise. Similarly, **Figure 10(b)** depicts the BER
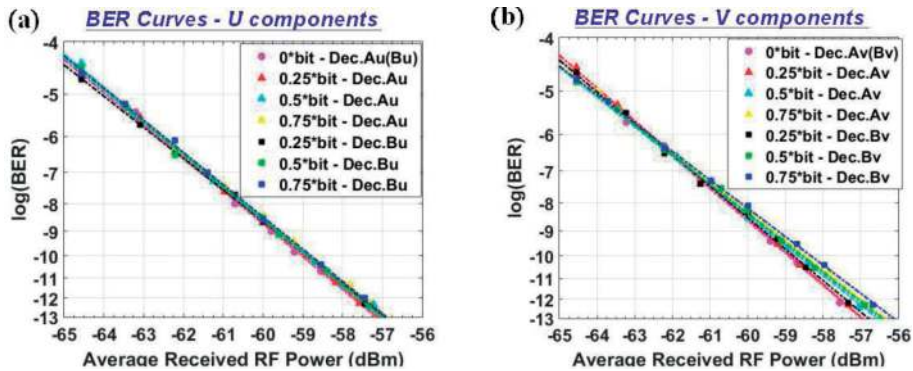
Figure 10. BER curves of the: (a) decoded data au and Bu and (b) decoded data Av and Bv components for various time offsets of 0.25bit, 0.5bit and 0.75bit in asynchronous operation.

curves of the decoded Av and Bv streams for time offsets equal to $0\tau_{symbol}$, $0.25\tau_{symbol}$, $0.5\tau_{symbol}$ and $0.75\tau_{symbol}$, showing error-free operations with negligible power penalty between the different BER curves. It is evident that the performance of the proposed AOPNC scheme remains similar even in the case of asynchronous packets reaching the network coder.

5. Conclusion

In this chapter, the concept of digital all-optical physical-layer network coding (AOPNC) was presented, targeting the future high-throughput radio-over-fiber (RoF) networks. In this scheme, the bitwise network coding (NC) is performed on the fly at the central office (CO) and the resultant packet is broadcasted at the wireless users, where the decoding takes place. The applicability of the AOPNC scheme between OOK-sub-carrier-modulated (SCM) data signals was confirmed by an experimental demonstration, employing a 10 GHz SC and an all-optical XOR gate as the digital NC encoder. An AOPNC scheme capable of performing the digital encoding and decoding between DQPSK-SCM data signals was also described. In this scheme the scenario of all optical encoding for 60 GHz SC used in mm-wave communications, followed by electrical decoding at the end users, was evaluated via physical-layer simulations. It should be noted that the described all-optical network Coding concept may in principle be applied also in RoF systems using DPSK-SCM and dual polarization (DP)-DQPSK-SCM modulation formats.

Acknowledgements

Author details

Charikleia Mitsolidou[1,2]*, Chris Vagionas[1,2], Dimitris Tsiokos[1,2], Nikos Pleros[1,2] and Amalia Miliou[1,2]

*Address all correspondence to: cvmitsol@csd.auth.gr

1 Department of Informatics, Aristotle University of Thessaloniki, Thessaloniki, Greece

2 Center for Interdisciplinary Research and Innovation, Aristotle University of Thessaloniki, Thessaloniki, Greece

References

[1] Cisco. Cisco Visual Networking Index: Global Mobile Data Traffic Forecast Update. 2016-2021 [Internet]. 2017. Available from: http://www.cisco.com/c/en/us/solutions/collateral/service-provider/visual-networking-index-vni/mobile-white-paper-c11-520862.html [Accessed: Jan 17, 2018]

[2] Ericsson. State and Future of the Mobile Networks [Internet]. 2017. Available from: https://www.ericsson.com/mobility-report/state-and-future-of-the-mobile-networks [Accessed: Jan 17, 2018]

[3] Ghazisaidi N, Maier M. Fiber-wireless (FiWi) access networks: Challenges and opportunities. IEEE Network. 2011;**25**:36-42. DOI: 10.1109/MNET.2011.5687951

[4] Novak D, Waterhouse RB, Nirmalathas A, Lim C, Gamage PA, Clark TR, Dennis ML, Nanzer JA. Radio-over-fiber Technologies for Emerging Wireless Systems. Journal of Quantum Electronics. 2015;**52**. DOI: 10.1109/JQE.2015.2504107

[5] Xu K, Wang R, Dai Y, Yin F, Li J, Ji Y, Lin J. Microwave photonics: Radio-over-fiber links, systems, applications. Photonics Research. 2014;**2**:B54-B63. DOI: 10.1364/PRJ.2.000B54

[6] Caballero A, Zibar D, Sambaraju R, Guerrero Gonzalez N, Tafur Monroy I. Engineering rules for optical generation and detection of high speed wireless millimeter-wave band signals. In: Proceedings of the European Conference on Optical Communications (ECOC '11); Geneva, Switzerland: IEEE; 18-22 September 2011

[7] Pleros N, Vyrsokinos K, Tsagkaris K, Tselikas ND. A 60 GHz radio-over-fiber network architecture for seamless communication with high mobility. IEEE/OSA Journal of Lightwave Technology. 2009;**27**:1957-1967. DOI: 10.1109/JLT.2009.2022505

[8] Chen L-K, Li M, Liew SC. Breakthroughs in photonics 2014: Optical physical-layer network coding, recent developments, and challenges. IEEE Photonics Journal. 2015;**7**. DOI: 10.1109/JPHOT.2015.2418264

[9] Liu ZX, Lu L, You L, Chan CK, Liew SC. Optical physical-layer network coding over fiber-wireless. In: Proceedings of the European Conference on Optical Communications (ECOC '13); London, UK: IEEE; 22-26 September 2013

[10] Manley ED, Deogun JS, Xu L, Alexander DR. All-optical network coding. IEEE/OSA Journal of Optical Communications and Networking. 2010;**16**:175-191. DOI: 10.1364/JOCN.2.000175

[11] Katti MS, Rahul H, Hu W, Katabi D, Médard M, Crowcroft J. Xors in the air: Practical wireless network coding. IEEE/ACM Transactions on Network. 2008;**16**:497-510. DOI: 10.1145/1159913.1159942

[12] Miller K, Biermann H, Woesner H, Karl H. Network coding in passive optical networks. In: Proceedings of the IEEE International Symposium on Network Coding (NetCod '10); Toronto, Canada: IEEE; 9-11 June 2010

[13] Fouli K, Maier M, Médard M. Network coding in next-generation passive optical networks. IEEE Communications Magazine. 2011;**49**:38-46. DOI: 10.1109/MCOM.2011.6011732

[14] Belzner M, Haunstein H. Network coding in passive optical networks. In: Proceedings of the European Conference on Optical Communications (ECOC '09); Vienna, Austria: IEEE; 20-24 September 2009

[15] Thinniyam RS, Kim M, Médard M, O'Reilly U-M. Network coding in optical networks with O/E/O based wavelength conversion. In: Proceedings of the Optical Fiber Communication Conference and Exposition/National Fiber Optic Engineers Conference (OFC/NFOEC '10); San Diego, CA, USA: OSA/ IEEE; 21-25 March 2010

[16] Qu Z, Ji Y, Bai L, Sun Y, Fu J. Key module for a novel all-optical network coding scheme. Chinese Optics Letters. 2010;**8**:753-756. DOI: 10.3788/COL20100808.0753

[17] Hisano D, Maruta A, Kitayama K. Demonstration of all optical network coding by using SOA MZI based XOR gates. In: Proceedings of the Optical Fiber Communication Conference and Exposition/National Fiber Optic Engineers Conference (OFC/NFOEC'13); Anaheim, CA, USA: OSA/ IEEE; 17-21 March 2013

[18] An Y, Ross FD, Peucheret C. All-optical network coding for DPSK signals. In: Proceedings of the Optical Fiber Communication Conference and Exposition/National Fiber Optic Engineers Conference (OFC/NFOEC '13); Anaheim, CA, USA: OSA/ IEEE; 17-21 March 2013

[19] Lu G-W, Hongxiang JQ, Gazi WYJ, Sharif M, Yamaguchi S. Flexible and re-configurable optical three-input XOR logic gate of phase-modulated signals with multicast functionality for potential application in optical physical-layer network coding. Optics Express. 2016;**24**:2299-2306. DOI: 10.1364/OE.24.002299

[20] Liu ZX, Li M, Lu L, Chan C-K, Liew SC, Chen L-K. Optical physical-layer network coding. IEEE Photonics Technology Letters. 2012;**24**:1424-1427. DOI: 10.1109/LPT.2012.2204972

[21] Mitsolidou C, Vagionas C, Ramantas K, Tsiokos D, Miliou A, Pleros N. Digital optical physical-layer network coding for mm-wave radio-over-fiber signals in fiber-wireless networks. IEEE/ OSA Journal of Lightwave TechnologyJ. Lightwave Technol. 2016;**34**:4765-4771. DOI: 10.1109/JLT.2016.2585673

[22] Caballero A, Zibar D, Monroy IT. Performance evaluation of digital coherent receivers for phase modulated radio-over-fiber links. IEEE/ OSA Journal of Lightwave Technology. 2011;**29**:3282-3292. DOI: 10.1109/JLT.2011.2167595

[23] Sambaraju R, Zibar D, Caballero A, Monroy IT, Alemany R, Herrera J. 100-GHz wireless-over-fibre links with up to 16 Gb/s QPSK modulation using optical heterodyne generation and digital coherent detection. IEEE Photonics Technology Letters. 2010;**2010**:1650-1652. DOI: 10.1109/LPT.2010.2076801

[24] Mitsolidou C, Pleros N, Miliou A. All-optical digital physical-layer network coding for DPSK mm-wave radio-over-fiber networks. In: Proceedings of the 19th International Conference on Transparent Optical Networks (ICTON '17); Girona, Spain. 2-6 July 2017

[25] Mitsolidou C, Pleros N, Miliou A. Digital all-optical physical-layer network coding for 2Gbaud DQPSK signals in mm-wave radio-over-fiber networks. Optical Switching and Networking. 2017; (In press) ISSN: 1573-4277. DOI: 10.1016/j.osn.2017.10.002

[26] Spyropoulou M, Pleros N, Miliou A. SOA-MZI-based non-linear optical signal processing: A frequency domain transfer function for wavelength conversion, clock recovery and packet envelope detection. IEEE Journal of Quantum Electronics. 2011;**47**:40-49. DOI: 10.1109/JQE.2010.2071411

[27] Chang K, Liu C. 1-100 GHz microwave photonics link technologies for next-generation WiFi and 5G wireless communications. In: Proceedings of the International Topical Meeting on Microwave Photonics (MWP '13); Alexandria, VA, USA: IEEE; 28-31 October 2013

[28] Vorreau P, Marculescu A, Wang J, Bottger G, Sartorius B, Bornholdt C, Slovak J, Schlak M, Schmidt C, Tsadka S, Freude W, Leuthold J. Cascadability and regenerative properties of SOA all-optical DPSK wavelength converters. IEEE Photonics Technology Letters. 2006;**18**:1970-1972. DOI: 10.1109/LPT.2006.880714

[29] Wang G, Yang X, Hu W. All-optical logic gates for 40Gb/s NRZ signals using complementary data in SOA-MZIs. Optics Commununications. 2013;**290**:28-32. DOI: 10.1016/j.optcom.2012.10.047

[30] Dennis ML, Nanzer JA, Callahan PT, Gross MC, Clark TR, Novak D, Waterhouse RB. Photonic upconversion of 60 GHz IEEE 802.15.3c standard compliant data signals using a dual-wavelength laser. In: Proceedings of the Annual Meeting of IEEE Photonics Society; Denver, CO, USA. 7-11 November 2010

[31] Seagraves E, Berry C, Qian F. Robust mobile WiMax preamble detection. In: Proceedings of the Military Communications Conference (MILCOM '08); San Diego, CA, USA: IEEE; 16-19 November 2008

[32] VPIphotonics. VPIphotonics Official Wedsite [Internet]. 2018. Available from: http://www.vpiphotonics.com/index.php [Accessed: Jan 17, 2018]

[33] Vagionas C, Fitsios D, Vyrsokinos K, Kanellos GT, Miliou A, Pleros N. XPM- and XGM-based optical RAM memories: Frequency and time domain theoretical analysis. IEEE Journal of Quantum Electronics. 2014;**47**:683-697. DOI: 10.1109/JQE.2014.2330068